SANDIA REPORT

SAND2020-10133 Printed September 2020



Microstructural Changes to Thermally Sprayed Materials Subjected to Dynamic Compression

Chad A. McCoy, Nathan W. Moore, and Andrew Vackel

Prepared by Sandia National Laboratories Albuquerque, New Mexico 87185 and Livermore, California 94550 Issued by Sandia National Laboratories, operated for the United States Department of Energy by National Technology & Engineering Solutions of Sandia, LLC.

NOTICE: This report was prepared as an account of work sponsored by an agency of the United States Government. Neither the United States Government, nor any agency thereof, nor any of their employees, nor any of their contractors, subcontractors, or their employees, make any warranty, express or implied, or assume any legal liability or responsibility for the accuracy, completeness, or usefulness of any information, apparatus, product, or process disclosed, or represent that its use would not infringe privately owned rights. Reference herein to any specific commercial product, process, or service by trade name, trademark, manufacturer, or otherwise, does not necessarily constitute or imply its endorsement, recommendation, or favoring by the United States Government, any agency thereof, or any of their contractors or subcontractors. The views and opinions expressed herein do not necessarily state or reflect those of the United States Government, any agency thereof, or any of their contractors.

Printed in the United States of America. This report has been reproduced directly from the best available copy.

Available to DOE and DOE contractors from

U.S. Department of Energy Office of Scientific and Technical Information P.O. Box 62 Oak Ridge, TN 37831

Telephone: (865) 576-8401 Facsimile: (865) 576-5728 E-Mail: reports@osti.gov

Online ordering: http://www.osti.gov/scitech

Available to the public from

U.S. Department of Commerce National Technical Information Service 5301 Shawnee Rd Alexandria, VA 22312

Telephone: (800) 553-6847 Facsimile: (703) 605-6900 E-Mail: orders@ntis.gov

Online order: https://classic.ntis.gov/help/order-methods/



ABSTRACT

Dynamic compression of materials can induce a variety of microstructural changes. As thermally-sprayed materials have highly complex microstructures, the expected pressure at which changes occur cannot be predicted *a priori*. In addition, typical *in-situ* measurements such as velocimetry are unable to adequately diagnose microstructural changes such as failure or pore collapse. Quasi-isentropic compression experiments with sample recovery were conducted to examine microstructural changes in thermally sprayed tantalum and tantalum-niobium blends up to 8 GPa pressure. Spall fracture was observed in all tests, and post-shot pore volume decreased relative to the initial state. The blended material exhibited larger spall planes with fracture occurring at interphase boundaries. An estimate of the pressure at which pore collapse is complete was determined to be ~26 GPa for pure tantalum and ~19 GPa for the tantalum-niobium blend under these loading conditions.

ACKNOWLEDGEMENTS

We thank Lena Pacheco, Josh Usher, Keith Hodge, and Randy Hickman for assembling the targets and operation of the VELOCE facility. We also thank Alex Hickman, Celedonio Jaramillo, and Christina Profazi for the metallographic imaging.

CONTENTS

1.	Intro	ductio	n	7		
2.	Expe	erimen	tal configuration	9		
			als			
	2.2.	Pulsed	-power load and diagnostics	10		
3.	Resu	ılts		13		
	3.1.		opic compression			
	3.2.	Metallo	ography	15		
		3.2.1.				
		3.2.2.				
		3.2.3.	Porosity	22		
4.	Cond	clusion	s	25		
Re	feren	ces		27		
Ap	pendi	x A.	Waveform data	31		
Ap	pendi	хB.	Overview images	39		
•	•					
DI	stiibu			43		
1 10	T O	E EIGI	IDEC			
8						
Fig		,				
_						
		2.2. Metallography				
Figure 3-2: The measured velocity profile for V543 shot shows no evidence of shock formation1 Figure 3-3: Cross-sectioned sample after mounting in epoxy and polishing (top-center portion of image)						
_						
_				Pa.22		
Fig				2.2		
T2:-						
_						
	Figure A-3: Simulated drive pressure for shot V543					

Figure A-8: Simulated sample pressure for shot V544	34
Figure A-9: Measured velocity profile in sapphire window for shot V545	35
Figure A-10: Sapphire window pressure for shot V544	
Figure A-11: Simulated drive pressure for shot V545	36
Figure A-12: Simulated sample pressure for shot V545.	36
Figure A-13: Measured velocity profile in sapphire window for shot V546.	37
Figure A-14: Sapphire window pressure for shot V546	37
Figure A-15: Simulated drive pressure for shot V546.	38
Figure A-16: Simulated sample pressure for shot V546.	38
Figure B-1: 200x magnification overview of untested tantalum sample	39
Figure B-2: 200x magnification overview of V543 tantalum sample compressed to 6.3 GPa	39
Figure B-3: 200x magnification overview of V545 tantalum sample compressed to 8.6 GPa	40
Figure B-4: 200x magnification overview of untested tantalum-niobium sample	40
Figure B-5: 200x magnification overview of V544 tantalum-niobium sample compressed to 6.2 C	ЭPа
Figure B-6: 200x magnification overview of V546 tantalum-niobium sample compressed to 7.4 C	GP a
	41
LIST OF TABLES	
Table I: Density, $ ho_0$, longitudinal sound speed, C_L , shear sound speed, C_S , and acoustic	
impedance, Z^3 , of sprayed tantalum and tantalum-niobium samples. Uncertainty is given as 1σ for all measurements of the tested samples as well as those reported in [7]	
Table II: Measured peak stress at aluminum panel-sapphire interface and simulated in-situ value	
for compressed tantalum and tantalum-niobium samples	14
Table III: Void percentages with and without fractured regions and relative porosity of	
compressed tantalum and tantalum-niobium samples	23

1. INTRODUCTION

The response of materials when subjected to dynamic loading has been a topic of research for much of the past century. However, for anisotropic materials, many questions remain about how such loading will impact the microstructure. These questions are particularly timely when considering the rise of additive manufacturing, in which the microstructures can differ from traditionally fabricated materials and tailored microstructures can be created[1]. Previous work has shown that the dynamic response of full-density additively manufactured materials can differ from wrought material[2].

Additional complexity is introduced by considering underdense materials with non-uniform pore distributions[3-5]. In these materials, the shock behavior can be impacted by grain anisotropy, interfacial roughness, and phase distribution in multi-phase materials. One source of non-uniform behavior is the scattering of transmitted waves due to interactions between materials with different acoustic impedances. In this case, the propagation of waves creates a sequence of rarefaction and compression waves which propagate in various directions throughout the material due to the stochastic orientation of internal interfaces. Because wave transmission occurs once the material across an interface becomes impedance matched (e.g. reaches continuous pressure and wavespeed conditions)[6], the stochastic spacing of pores will result in spatially-varying stress and density inside the material.

To leverage existing knowledge on the behavior of materials under dynamic loading and recent work to understand non-uniform materials [7], we chose to study porous tantalum. Solid tantalum has been extensively studied under shock [8-14] and ramp [15-19] compression, such that its behavior is well-constrained and variations in behavior identified in this work could be directly attributed to the porous structure studied. Previous work found that the coefficient of restitution varies at low-strain rates due to asperity crushing, and similar behavior would be expected under dynamic loading at higher strain-rates. More recently, shock-wave loading of porous tantalum coatings identified a complex shock behavior with a rounded wave-profile that is likely due to crushing of voids within the sample [7]. However, no measurable spall strength was able to be determined and an upper bound was estimated to be <20 MPa. Additionally, soft-recovery of intact samples of this material was not possible due to brittle fracture for pressures above 50 MPa[20]. Ramp compression is a less-damaging process due to its lower strain-rate, but also enables encapsulation of the sample within a copper cylinder. Encapsulation allows for the sample to fracture or spall without separating into pieces, thereby enabling inspection of the recovered material.

Porous tantalum structures were fabricated using thermal spraying. In this technique, a tantalum feed powder is fed into a plasma torch and sprayed onto a substrate. The plasma torch consists of a high-velocity plasma jet which rapidly heats and accelerates the particles, such that they are deposited as molten "splats" on the substrate[21]. This method has been used to create non-corrosive coatings of large rare-earth magnets and chemical reactors[22]. The method builds up a coating layer-by-layer and can efficiently produce large thicknesses (>1 mm).

Additionally, samples of co-sprayed tantalum-niobium blends were prepared to allow a direct comparison to materials tested in previous gas-gun experiments [7]. The inclusion of niobium has been demonstrated to increase strength to refractory metals in alloys [23], however the spray process tends to form discrete regions with minimal alloying. On the other hand, the difference in melting temperature may influence the interphase adhesion between the tantalum and niobium regions of the coating, and it remains to be determined if the presence of niobium or other metal phases alters the mechanical strength or behavior under dynamic compression. Testing this material also served to help

nderstand dynamic deformation at interfaces between dissimilar metals, which could not be achieved with pure tantalum.	1

2. EXPERIMENTAL CONFIGURATION

2.1. Materials

Samples of tantalum and tantalum-niobium blend were produced using an air plasma spray (APS) process. Similar to other thermal-spray processes, this method creates a layered microstructure where boundaries between splats can fracture on shock loading, owing to limited alloying and interaction between adjacent splats [24-26]. For air-sprayed materials in particular, significant quantities of oxides can be formed due to the reactive nature of tantalum and niobium at high temperature [27]. Oxides and interstitially absorbed nitrogen embrittle the sprayed coating which produces potential fracture surfaces [28]. Post-shot examination of fracture surfaces and spall planes can determine if fracture followed the weakened splat boundaries or crossed individual splats.

Details of the samples fielded in these experiments are given in Table I. For these experiments, 5.8 mm diameter samples were cut from flat plates, which were sprayed onto aluminum substrates, using electrical discharge machining with a 4-mil brass wire. These samples were cut and polished for a final thickness of 1.25 mm. An image of a sample before polishing is shown in Figure 2-1. The spray process and equipment used to produce the samples is described in detail in reference [7].



Figure 2-1: Unpolished 5.8 mm diameter sprayed sample

Table I: Density, ρ_0 , longitudinal sound speed, C_L , shear sound speed, C_S , and acoustic impedance, Z^3 , of sprayed tantalum and tantalum-niobium samples. Uncertainty is given as 1σ for all measurements of the tested samples as well as those reported in [7].

Material	ID (spray date/run)	$ ho_0$ (g/cm ³)	C_L (m/s)	C_S (m/s)	Z^3 (kg/m ² -s/10 ⁶)
Tantalum	20180416r01A	12.53±0.08	2102±17	1404±5	26.8±0.3
Tantalum-niobium	20180425r01A	10.59±0.09	2534±8	1691±8	26.9±0.3

Panels for the pulsed power driver were machined from 6061-T6 aluminum with a lithium fluoride (Lattice Electro Optics, Fullerton, CA) window bonded into the drive panel using AngstromBond 9110 LV (Fiber Optic Center, New Bedford, MA). The LiF window had an Al spot coating on the

drive surface and anti-reflective coating for 532 and 1550 nm on the back surface. The floor thickness of the aluminum panels was 3.0 mm and the counterbore diameter in which the LiF window and recovery capsule were mounted was 23.0 mm. LiF windows used in these experiments were 17 mm diameter by 8 mm thick. The recovery capsule was machined from OFHC copper with the sample bonded inside using AngstromBond.

2.2. Pulsed-power load and diagnostics

Experiments were conducted on the VELOCE pulsed power generator at the Dynamic Integrated Compression Experimental (DICE) facility located at Sandia National Laboratories. The VELOCE generator is a high-voltage, medium-current generator designed for isentropic compression experiments [29]. In this work, the machine is charged to a voltage of 55 or 65 kV, which generates a current of 1.95 or 2.65 MA that is driven through the target.

Targets for these experiments used a strip-line design where one panel provided a drive measurement, and the other panel housed the recovery capsule. A schematic of the target is given in Figure 2-2. In the strip-line geometry, the current is driven up one panel then crosses at a shorting cap at the end to travel down the other panel. The current density, \vec{J} , induces a magnetic field between the panels, \vec{B} . Interaction between the current density and magnetic field produces the $\vec{J} \times \vec{B}$ Lorentz force which accelerates the panels away from each other. The acceleration due to this force drives the panels to velocities >100 m/s over tens of nanoseconds. Because the current is uniform on both sides, the magnetic force measured on the drive side is the same as that experienced by the recovery capsule. This enables use of simulations to relate the measurement of the wave profile on the drive side to an expected wave profile in the sample.

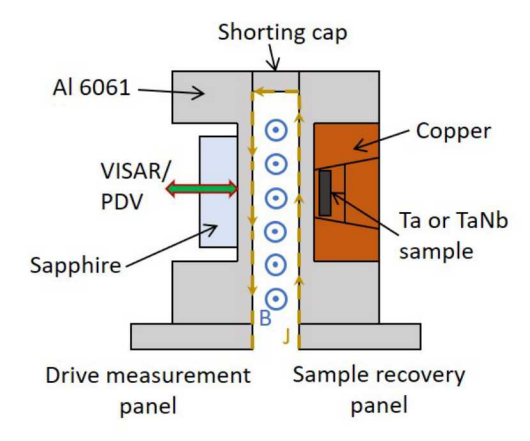


Figure 2-2: Target schematic showing drive and recovery panels

The recovery capsule (Figure 2-3) consisted of a copper cup which housed the sample and copper anvil to maintain pressure that propagated through the sample. This assembly was mounted in a larger copper ring that was bonded into the panel as shown in Figure 2-4.

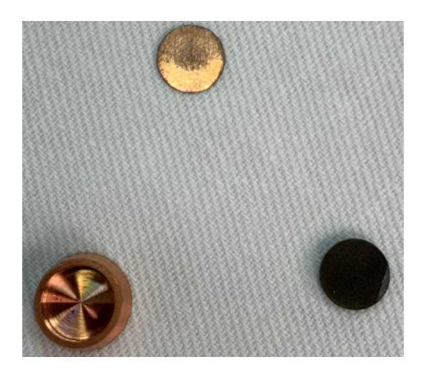


Figure 2-3: Copper cup (left), cap (top) and sample (right) prior to assembly of recovery capsule



Figure 2-4: Assembled sample recovery (left) and drive (right) panels

The velocity history of the drive panel was measured using both a velocity interferometry system for any reflector (VISAR)[30, 31] and photonic doppler interferometry (PDV)[32]. A single probe (Romulan probe, Berkshire Photonics, Washington Depot, CT) was mounted to the back of the LiF window to look at the Al spot coating. The Romulan probe consists of four 200 μ m multi-mode fibers for VISAR and three 9 μ m single-mode fibers for PDV. The end of the probe is flat-polished barefiber so separate fibers carry the send and receive signals. VISAR measurements were made using a 532 nm Nd:YAG laser. The VISAR setup used two velocity-per-fringe (VPF) settings to remove the 2π phase ambiguity present in jumps due to shocks. The vacuum VPF sensitivities were 40 and 60 m/s, which correspond to 22.4 and 33.6 m/s in the sapphire window, respectively. The density-dependent sapphire window index was taken from Jensen *et al*[33]. Analysis was carried out using the PointVISAR program[34]. The PDV data was analyzed using the program SIRHEN using a 3 ns window[35].

3. RESULTS

The discharge of the VELOCE capacitor bank drives a steady ramp wave into the panel, shocklessly compressing the sample and drive panels along a path close to the principal isentrope. Four experiments were carried out to isentropically compress and recover air-sprayed tantalum (AS-Ta) and tantalum-niobium (AS-TaNb) to pressures >5 GPa. Two experiments were carried out on each material with charge voltages of 55 and 65 kV. Post-shot recovery of the samples was used to understand microstructural changes to the sample induced by dynamic compression.

Because the samples are brittle and porous, the expected microstructural changes were spall fracture and pore collapse. To first order, ramp compression achieves a uniform peak stress throughout the sample. This allows for understanding of stress-dependent phenomena such as pore collapse and spall. Metallographic imaging was used to examine the interior of cross-sectioned samples to determine the post-shot porosity of the sample and whether spall occurred.

3.1. Isentropic compression

Wave profiles on the drive side of the target were measured using VISAR and PDV. Using the drive wave profile, backwards simulations in the 1D magnetohydrodynamics code LASLO were used to determine the condition at the drive surface. This drive condition was then applied to the sample side of the target and forward simulations predicted the time dependent pressure present in the sample. Figure 3-1 illustrates the process used to determine the peak sample pressure. Peak sample pressures achieved are given in Table II. The peak stress in sapphire was determined from the principal isentrope calculated using SESAME 7411 equation of state table. Simulations of the sample used a Mie-Grüneisen equation of state with the Hugoniot as the reference curve. Tantalum and tantalumniobium Hugoniots were taken from the stress-density relations given in reference [7].

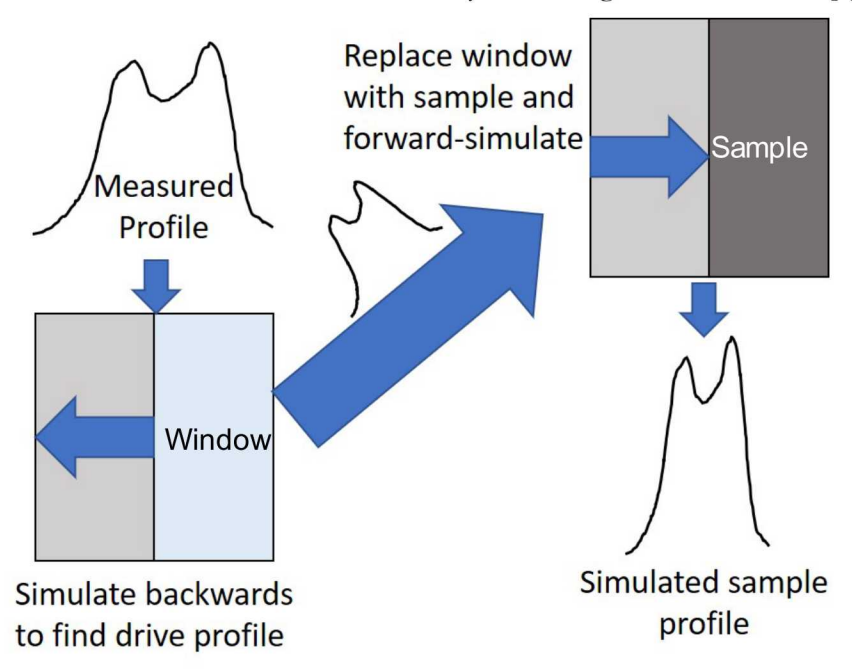


Figure 3-1: Analysis technique used to determine wave stress history in sample

Table II: Measured peak stress at aluminum panel-sapphire interface and simulated *in-situ* value for compressed tantalum and tantalum-niobium samples

Material	Shot	Peak Stress in sapphire	Peak Stress in sample
Tantalum	V543	5.6 GPa	6.3 GPa
Tantalum	V545	7.6 GPa	8.6 GPa
Tantalum-niobium	V544	5.6 GPa	6.2 GPa
Tantalum-niobium	V546	6.7 GPa	7.4 GPa

The ramp waves that compressed the samples had a nominal rise time of \sim 400 ns. Over this duration, the panels accelerated outwards to drive the steady compression of the sample. From the averaged drive measurement on shot V543 (Figure 3-2) no shock is seen in the wave profile. The hydrodynamic simulations of these experiments only considered the duration where the wave profile implied positive pressure when determining the drive condition. The later-time negative velocity and pressure was excluded as not significant to the experimental objective of determining the peak state in the sample. Interface velocity and pressure profiles for the sapphire windows, as well as drive and sample pressure profiles are given in Appendix A. The hydrodynamic simulations used to identify the conditions in the sample found that the peak magnetic pressure applied to the panel was \sim 10-15% less than the peak pressure in the window, which would be expected due to sapphire having higher impedance than aluminum. In addition, the second peak in the drive pressure was greater than the first peak due to wave attenuation as it transited the compressed material.

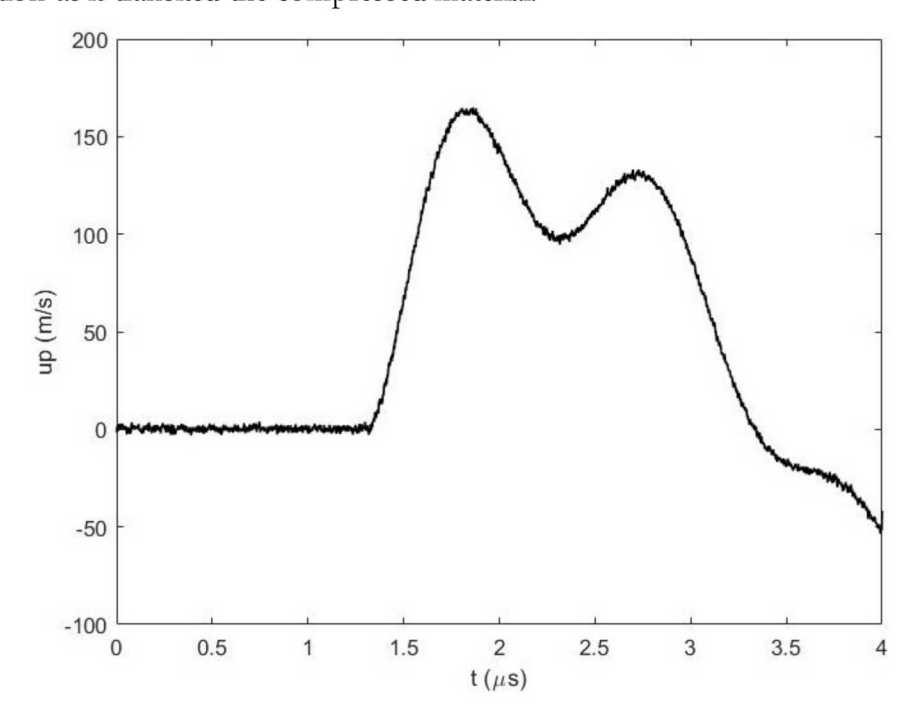


Figure 3-2: The measured velocity profile for V543 shot shows no evidence of shock formation

Simulated peak pressures in the samples exceeded those of the sapphire windows by \sim 15%. In addition, the high impedance suppressed the second peak such that the drive shows a peak followed by a release to an approximately constant pressure. Interestingly, the peak state reached in the tantalum and tantalum-niobium when driven by the same pressure were almost identical. This implies that the compression of the material under isentropic loading is less sensitive to the difference in initial density than the Hugoniot, and the smaller void fraction in the blended material may compensate for the initial density difference.

3.2. Metallography

The sample recovery capsules all remained intact throughout the experiment. Due to plastic deformation of the capsule and sample, the samples were unable to be removed from the capsule by non-destructive means. Hence the entire capsule was provided to the metallography lab at Sandia National Laboratories for cross-sectioning and high-resolution imaging. In addition to the recovered capsules from the four shots, an untested sample of each material was also provided as a control. This control was used to determine the initial porosity of the sample and provide insight into whether connected voids existed throughout the coating. To have the control sample be most representative of the other materials, it was requested for the samples to be cut as close as possible to each other from the substrate.

Samples were cross-sectioned through the center and polished to produce a smooth surface for imaging. An example of a cross-sectioned sample and capsule is shown in Figure 3-3. Three subsets of metallographic imaging were carried out for each sample: 1. A stitched 200x overview of the entire sample to examine whether spall occurred and the size of the spall planes; 2. 500x imaging of entire sample; and 3. 1000x imaging of areas where spall did not occur to calculate post-shot porosity of the sample. The 200x overview images can be found in Appendix B.

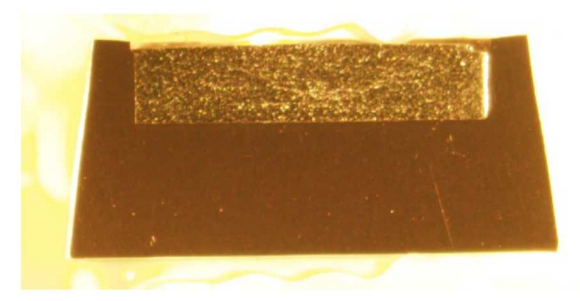


Figure 3-3: Cross-sectioned sample after mounting in epoxy and polishing (top-center portion of image)

3.2.1. Tantalum

The overview image (Figure B-1) of the untested tantalum sample exhibits the layered microstructure that is expected for plasma sprayed materials. From the image, small voids are approximately uniformly distributed throughout the entire sample with larger voids appearing in clusters. Because splats deposited through the spray process have little interaction beyond cooling on the surface of the previously deposited layer, there should be no predisposition for voids to form near a pre-existing void. In this regard, the clustering may be a sign that the voids visible in the image spread to a larger extent at different depths into the sample such that the cooling splats did not have material upon which to adhere. Because fracture surfaces have been shown to initiate at voids[36], this clustering may produce preferential loci where fracture could occur under compression and tension.

In addition to the clustering of larger voids, the metallographic imaging identified a large copper inclusion in the sample (Figure 3-4). Additional copper inclusions were also identified in the sample. The presence of copper inclusions is likely related to the copper nozzle used in the plasma torch. Because tantalum's melting point is 3290 K, heat from the plasma torch necessary to melt the tantalum powder is significantly greater than the melting point of copper (1358 K). The nozzle also acts as the anode and can be prone to wear from DC arc attachment used to create the plasma used to melt the powder feedstock. As the amount of copper is very small (<<1%), it is unlikely to have had any impact on the mechanical behavior of the sprayed tantalum.

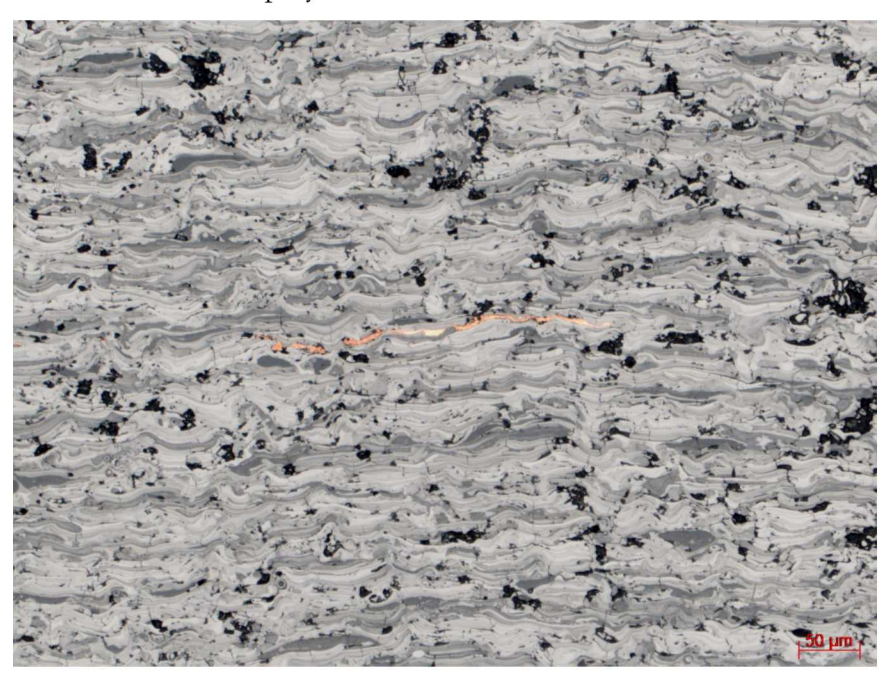


Figure 3-4: A large copper inclusion was identified in the untested tantalum sample.

At the higher resolution, the metallographic imaging showed thin voids between splats which indicate that layers did not all bond to one another (Figure 3-5). These layers are likely related to the formation of oxides on the surface of the molten tantalum droplets as identified using energy-dispersive x-ray spectroscopy in reference [20]. Additional features that became distinct at high resolution are small cracks that run vertically through the sample and transect individual splats; however, they constitute a smaller volume fraction than the voids between splats. These cracks may be the result of strain-relief in individual splats during the rapid quenching that occurs during deposition, and are more prevalent in materials sprayed in oxygen- or nitrogen-rich environments (such as air). The cracks also have jagged edges which are indicative of brittle fracture on cooling of the splats. This implies that under stress the sample could exhibit brittle fracture with fracture surfaces oriented laterally across the sample rather than in the direction of the compressive wave; however, voids and potential fracture surfaces are seen in both directions.

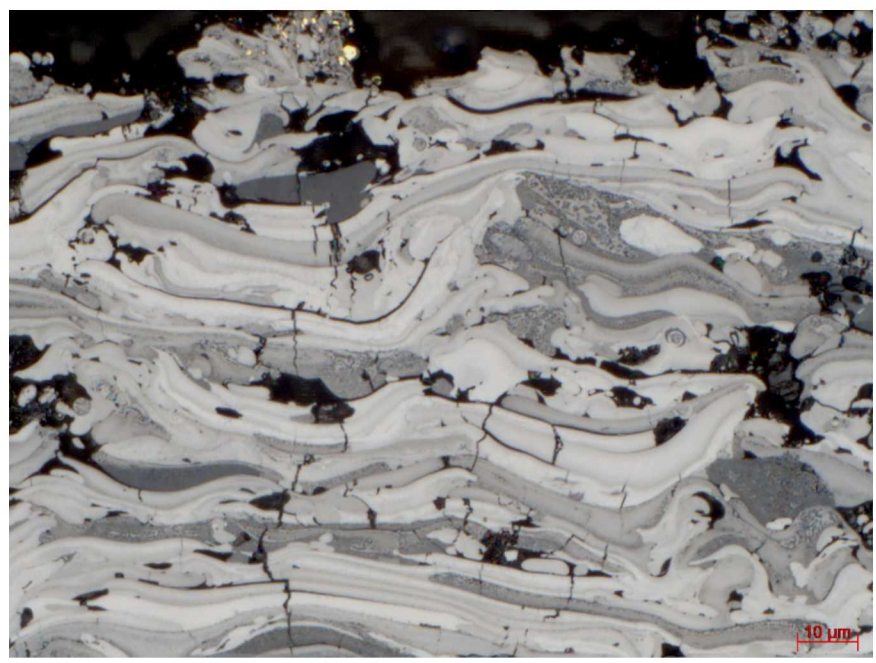


Figure 3-5: 1000x magnification image of untested tantalum sample

The first shot, V543 compressed a tantalum sample to 6.3 GPa. From the overview image (Figure B-2), the sample spalled, with the maximum tension experienced ~800 µm from the front surface of the sample. Additional spall planes formed at various depths ranging from ~200-1050 µm from the front surface. Interestingly, no spall planes could be identified within 200 µm of either surface. Because this image does not define the depth of the spall planes or other planes present in the sample, there is not enough evidence to conclude that spall did not occur in the vicinity of the surface. More careful examination of the spall planes indicates that failure occurred due to brittle cleavage fracture along splat boundaries. This observation parallels typical behavior of brittle materials where cleavage occurs at grain boundaries [9, 37, 38], however in the sprayed material, the splat interface clearly has less strength than the grain interface

The pressure at which fracture occurred is likely less than that for both the solid and porous tantalum samples produced by selective laser melting[9]. In that study, the lowest spall strength (of 3.3 GPa) was found to be for the through-thickness samples, which were oriented 90 degrees to the strain direction in that work. For in-plane samples, the spall strength was ~4-4.5 GPa. Here, because the peak stress was 6.3 GPa, the spall strength in our samples may have been less because the rarefaction waves propagating through the sample decay in strength over a longer duration than typical in a shock experiment. It remains unknown, however, if the spall strength was as low as estimated from Moore et al [7], where only an upper bound of ~20 MPa was estimated.

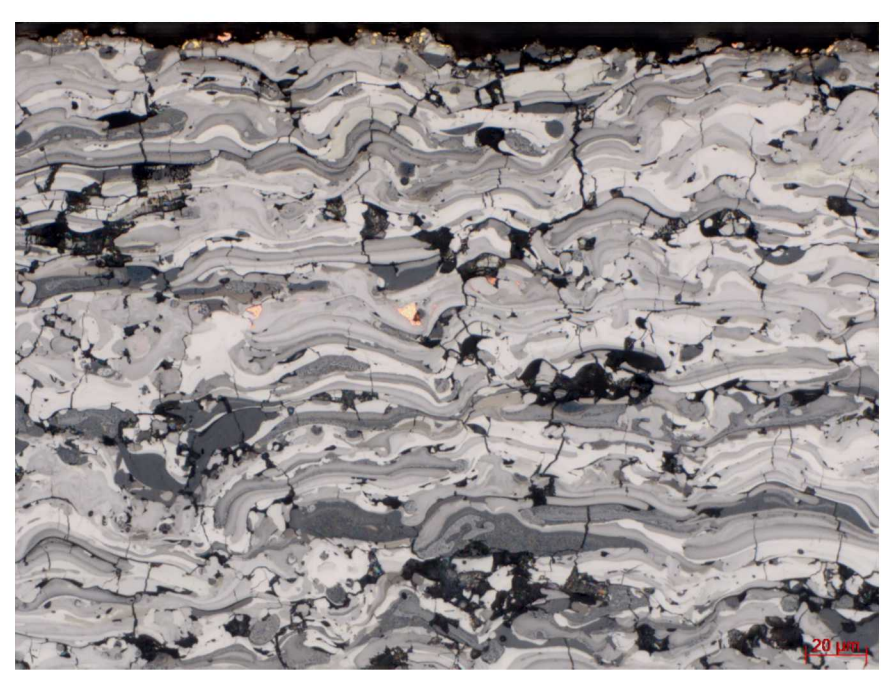


Figure 3-6: 500x magnification image of V543 tantalum sample compressed to 6.3 GPa

At high resolution, the tested tantalum sample (Figure 3-6) shows a greater density of fine cracks transecting splats than the untested sample. While the samples were not taken from the same location on the substrate, they were all cut adjacent to one another and would have experienced similar strains when cooling, so overall crack and void density should be similar. The increased crack density is therefore believed to be related to the ramp-compression experiment. These cracks transit splats cleanly and show no evidence of curvature within splats, which indicates that they are the result of brittle fracture, meaning that little ductility remained in the individual splats after the spray process.

The tantalum sample compressed to the highest stress, V545 (Figure B-3), showed fewer fracture surfaces than present after shot V543. However, what is clear from the overview is that the strain applied to the sample during compression and release caused significant fracturing of the sample. A large crack extends through the entirety of the center of the sample and additional cracks also run in the orientation of the stress wave and spray direction. The lack of significant spall planes such as those seen in the lower-stress experiment indicate that the cracks likely formed under compression rather than tension. At these cracks, when the tensile wave entered the sample, lateral unloading would be possible, which likely decreased the strain on the individual splats and prevented spall.

Towards the edges of the sample, little cracking occurred and there are fewer large voids that can be identified from the image. This provides evidence that pore collapse may have occurred in the sample, and a quantitative measurement of relative porosity is discussed in section 3.2.3.



Figure 3-7: 500x magnification image of crack in V545 tantalum sample



Figure 3-8: 500x magnification image of small void fraction at edge of V545 tantalum sample

At 500x resolution (Figure 3-7) the crack in the sample was measured to be 33 µm wide at its largest point. This width exceeds the typical thickness of the splats by 3-5x and is about the same width as the largest individual voids identified in the untested sample. The crack cleanly cleaves splats as well as follows splat boundaries which further supports the conclusion from the V543 sample that the tantalum sample fractured in a brittle manner. As the crack opened, release of the lateral pressure into the surrounding material would be required. As the cell holding the sample was made of cast copper, which still has strength at these conditions, the expansion of the crack likely contributed to the collapse

of voids near the edge of the sample. The porosity of the sample was determined from image analysis and compared to the untested sample in section 3.2.3.

3.2.2. Tantalum-niobium blend

For the untested sample (Figure B-4), no qualitative differences were identified from the pure tantalum sample. Both samples exhibit the same layered microstructure and uniform distribution of small pores. In the tantalum-niobium sample, larger voids appear more randomly distributed rather than in clusters, but this may be related to the location of the cross-sectioned slice rather than any characteristic difference from the inclusion of niobium.

At high resolution, the flat voids between splats appear more prevalent in the tantalum-niobium sample. This indicates that in the air-spray process, the formation of oxide layers on tantalum and niobium decreases adhesion between individual splats, rather than increasing strength as would be expected for an alloy. In addition, the increased prevalence of interfacial voids implies that the cosprayed material would be more likely to spall at lower pressure than the pure tantalum material.



Figure 3-9: 500x magnification image of untested tantalum-niobium sample

The hypothesis that spall strength is lower in the co-sprayed material is borne out in the result from the V544 test at 6.2 GPa. In the overview image (Figure B-5), large spall planes exist throughout the depth of the sample. These spall planes follow interfaces between splats and are indicative of brittle cleavage fracture due to oxide inclusion. Similar to the pure tantalum, failure at splat boundaries indicates that for the sprayed material, the interface between adjacent splats is the weakest point in the coating.

In addition to spall failure at the interface between splats, cracks oriented with the strain direction are also present in the sample. The combination of strain-oriented cracks and spall planes transits the entirety of the sample, such that all failure locations are connected. As a result, the copper encapsulation of the sample is the only aspect keeping the sample from fragmenting into multiple small pieces which would prohibit cross-sectioning and metallographic imaging. As the drive condition

was nominally the same as the V543 test of pure tantalum, it can be concluded that the co-sprayed sample is weaker than the pure material when sprayed in air.

At high-resolution, examination of the cracks oriented with the strain direction showed that in cases where the crack transited splats, the splats generally cleaved along grain boundaries through brittle fracture. In a very small fraction (<1%), there is evidence of possible ductility within a splat. This was not identified in the tantalum sample, but in tests of nanoscale-sized samples of refractory metals, niobium was found to maintain some ductility at conditions beyond the ductile-to-brittle transition in tantalum [39].



Figure 3-10: 500x magnification image of V544 tantalum-niobium sample compressed to 6.2 GPa

The highest stress TaNb shot, V546, reached a stress of 6.2 GPa. In this experiment, the spall planes that formed were smaller and less numerous than in the lower pressure shot. From the overview image (Figure B-6), large spall planes formed by the drive surface of the sample and extended across the bulk of the sample. These spall planes are both connected by large cracks and a significant bulge is visible on the front surface above the planes. The bulge on the surface was formed by the release of material, indicating that under tension the spall planes opened sufficiently to shear material around the target center.

A significant difference in the behavior from the lower-stress shot is seen at the bottom two-thirds of the sample. Instead of having spall planes form under tension as the stress relaxed from the peak state, large cracks oriented along the strain direction were formed. These cracks were also identified in the high-stress test with pure-tantalum, V545. The cracking of the sample under compression may have provided an avenue for strain relief resulting in the sample withstanding spall fracture. However, while these cracks may have enhanced the resistance to spall, the formation of large voids through cracking during the compressive wave may have resulted in lower overall strength as the sample would then not have withstood tensile forces in the absence of the copper cell during conventional shock loading.

When examining crack formation at high resolution (Figure 3-11), it is evident that cracks opened both laterally and in the direction of the compressive wave. At segments where the crack travelled

laterally, the failure follows a splat interface, which is expected from the results of the other tested samples. As the splat interfaces appear to be the preferential locations for crack initiation, undissipated tensile forces may have resulted in failure along those interfaces. At some of the interfaces, it appears that a pre-existing void followed the boundary to produce a failure point which the crack followed. Within splats, the crack cleanly sheared the tantalum and niobium materials with no necking or ductile behavior identified in the transition. This indicates that at the peak stress of this shot, the force which resulted in shearing of splats exceeded the ductile-to-brittle transition for both tantalum and niobium or their oxides. Translation of splats across the crack implies that the stress was non-uniform across the sample at a time after the crack initiated, with material to the right of the crack translated by $\sim 2-3$ μ m relative to the left side. This could be a result of shearing or spallation in a portion of the sample.

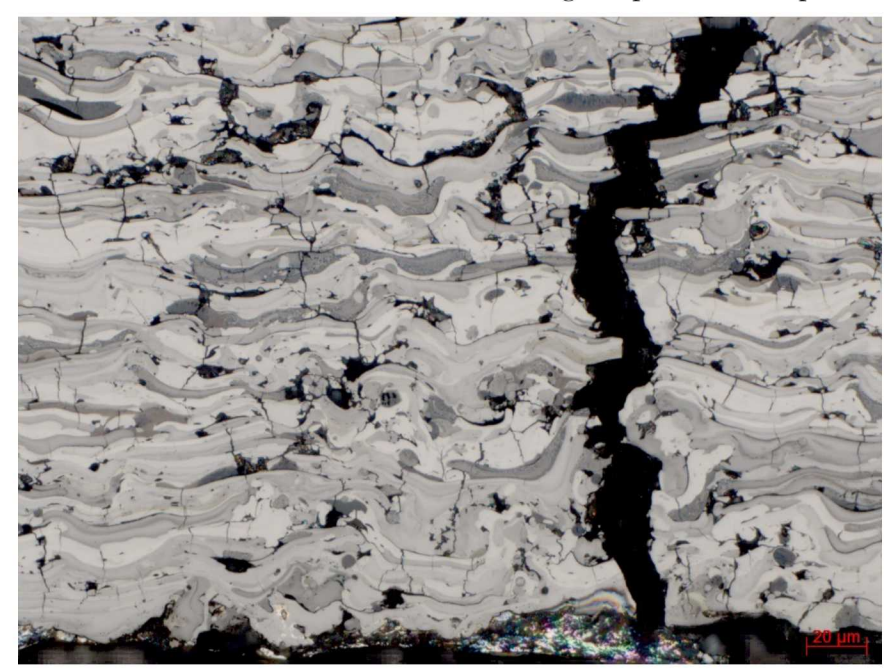


Figure 3-11: 500x magnification image of V546 tantalum-niobium sample compressed to 7.4 GPa

3.2.3. Porosity

The void fraction was estimated from the metallographic imaging through image analysis. As voids in the image shows up as black, the images were analyzed in MATLAB and a threshold was applied to define regions as void based on the absolute intensity of each pixel. This method was also applied to count singular bright pixels within a void as being part of the void by assuming that a single pixel is likely related to the preparation of the samples for imaging. An example image and its void region is shown in Figure 3-12.

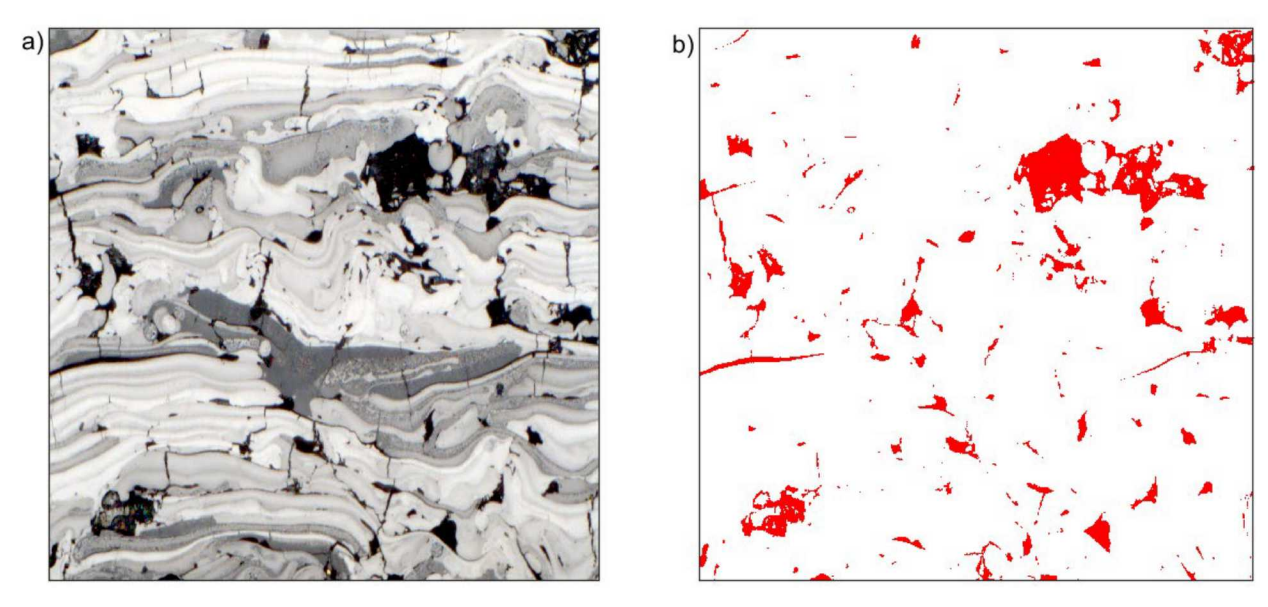


Figure 3-12: Demonstration of threshold to convert from (a) original 1000x image to (b) void fraction

The 500x images of the entire sample were used to determine an overall void percentage, with the 1000x images of regions where failure did not occur scaled to match the 500x images. This was done because the 1000x and 500x images determined different void percentages because the 500x images systematically underestimated the size of voids due to the presence of edges within individual pixels. If the pixel included the edge of a void, the light return from the metal surface was sufficient for the region to be identified as metal rather than as void. Measurement of the overall void percentages and relative porosity outside of failure regions are given in Table III; in this case we consider the relative porosity to be the porosity of the sample outside the fracture region divided by that of the untested sample. The systematic uncertainty in determining the porosity was assumed to be 0.5%. A more extended discussion of uncertainties of void percentage determination using 2D image analysis was provided in [40]. For the purpose of this study, the method is sufficient for comparing differences between untested and compressed samples.

Table III: Void percentages with and without fractured regions and relative porosity of compressed tantalum and tantalum-niobium samples

Material	Sample	Peak stress	Total void	Void excl. fractured regions	Relative Porosity
Та	Untested	0.0 GPa	7.9±0.5%	N/A	1
Та	V543	6.3 GPa	8.2±0.5%	5.8±0.9%	0.73±0.12
Та	V545	8.6 GPa	8.8±0.5%	5.4±0.6%	0.69±0.09
TaNb	Untested	0.0 GPa	6.2±0.5%	N/A	1
TaNb	V544	6.2 GPa	9.6±0.5%	4.2±1.2%	0.68±0.20
TaNb	V546	7.4 GPa	9.9±0.5%	3.8±0.8%	0.62±0.14

Total void percentages of the untested materials found in this study are similar to those previously measured by Moore et al[40]. When examining the tested samples, the TaNb samples had significantly higher total void fractions than the pure Ta when compared to the untested samples. The porosity of the compressed samples decreases with increasing peak stress, which is expected as the voids will collapse, however the uncertainty in relative porosity makes it difficult to fit a trend to the results. The relationship between porosity and peak stress is given in Figure 3-13. Linear extrapolation of these results implies that pore collapse may complete at 26.2 GPa in Ta and 19.4 GPa in TaNb, which is well above the conditions achievable on the VELOCE driver. Recovery on a larger system, such as THOR[41], or in-situ x-ray imaging during compression may therefore be required to determine the stress at which pore collapse is complete.

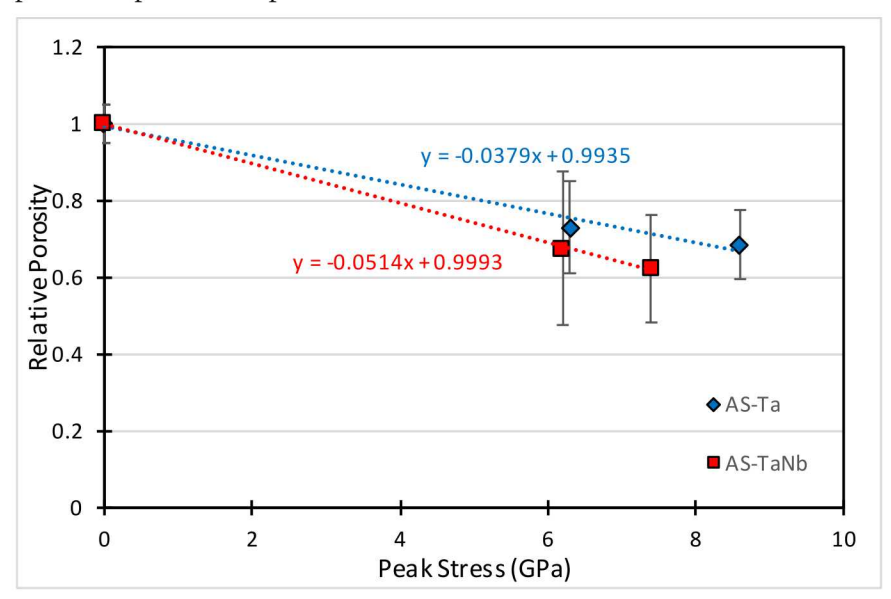


Figure 3-13: Relative porosity vs. peak stress for porous sprayed tantalum and tantalum-niobium

4. CONCLUSIONS

Experiments were conducted to recover air-plasma-sprayed tantalum and tantalum-niobium samples after being subjected to quasi-isentropic loading. The peak stress in the samples ranged from 6 to 8 GPa and was determined from hydrodynamic simulations based on measurement of the drive panel response. Cross-sectioning and metallography was conducted on the recovered samples to identify microstructural changes that occurred during the experiment.

In both samples, the lowest-stress fracture mechanism was determined to be brittle fracture along the splat boundaries. The tantalum samples exhibited smaller spall planes and an increased amount of strain-oriented cracking than the tantalum-niobium blend. This behavior implied that the splat boundary between different species of metal was weaker than the boundary between like-metals. The cracks oriented with the strain direction were more likely to cross individual splats and showed characteristics of brittle fracture along grain boundaries. One possibility is that significant oxygen or nitrogen uptake occurred during the spray process, and that it was not localized to the splat boundary. Minimization of the oxide content in the sprayed coating should provide a path forward to increasing coating strength. This may be achievable with controlled-atmosphere plasma-spray (CAPS), of which samples will be tested in FY 2021.

Examination of areas away from the fracture surfaces was used to estimate the relative porosity of the compressed samples when compared to an untested control sample. The porosity was found to decrease with increasing peak stress. Extrapolating the porosity as a function of stress suggested that pore collapse may complete at 19 GPa for the tantalum-niobium blend and 26 GPa for the pure tantalum. These conditions are beyond what is capable on the VELOCE driver and could therefore not be tested.

REFERENCES

- [1] W. J. Sames, F. A. List, S. Pannala, R. R. Dehoff, and S. S. Babu, "The metallurgy and processing science of metal additive manufacturing," *International Materials Reviews*, vol. 61, pp. 315-360, 2016.
- [2] J. L. Wise, D. P. Adams, E. E. Nishida, B. Song, M. C. Maguire, J. Carroll, *et al.*, "Comparative shock response of additively manufactured versus conventionally wrought 304L stainless steel," *AIP Conference Proceedings*, vol. 1793, p. 100015, 2017.
- [3] Z. P. Tang, W. Liu, and Y. Horie, "Numerical investigation of pore collapse under dynamic compression," *AIP Conference Proceedings*, vol. 505, pp. 309-312, 2000.
- [4] B. Branch, A. Ionita, B. M. Patterson, A. Schmalzer, B. Clements, A. Mueller, *et al.*, "A comparison of shockwave dynamics in stochastic and periodic porous polymer architectures," *Polymer*, vol. 160, pp. 325-337, 2019.
- [5] B. M. Patterson, L. Kuettner, N. Cordes, K. Henderson, M. Herman, C. Welch, et al., "Probing Material Morphology and Deformation as a Response to in situ Loading using X-ray Tomography," *Microscopy and Microanalysis*, vol. 25, pp. 374-375, 2019.
- [6] Y. B. Zel'dovich and Y. P. Raizer, *Physics of Shock Waves and High-Temperature Hydrodynamic Phenomena*: Dover Publications, 2002.
- [7] N. W. Moore, G. R. Chantler, A. Vackel, J. L. Wise, R. Pokharel, and D. Brown, "Stochastic shock observations from plate impact of porous refractory metals," Sandia National Laboratories, Albuquerque, NM SAND2019-10376, 2019.
- [8] J. Brown and J. Shaner, "Rarefaction velocities in shocked tantalum and the high-pressure melting point," Texas A and M Univ., College Station (USA); Los Alamos National Lab., NM (USA)1983.
- [9] D. R. Jones, S. J. Fensin, B. G. Ndefru, D. T. Martinez, C. P. Trujillo, and G. T. GrayIII, "Spall fracture in additive manufactured tantalum," *Journal of Applied Physics*, vol. 124, p. 225902, 2018.
- [10] A. C. Mitchell and W. J. Nellis, "Shock Compression of Aluminum, Copper, and Tantalum," *J. Appl. Phys.*, vol. 52, pp. 3363–3374, 1981.
- [11] W. J. Nellis, A. C. Mitchell, and D. A. Young, "Equation-of-state measurements for aluminum, copper, and tantalum in the pressure range 80–440 GPa (0.8–4.4 Mbar)," *Journal of applied physics*, vol. 93, pp. 304-310, 2003.
- [12] C. Dai, J. Hu, and H. Tan, "Hugoniot temperatures and melting of tantalum under shock compression determined by optical pyrometry," *Journal of Applied Physics*, vol. 106, p. 043519, 2009.
- [13] S. V. Razorenov, G. Garkushin, G. I. Kanel, and O. N. Ignatova, "The spall strength and Hugoniot elastic limit of tantalum with various grain size," *AIP Conference Proceedings*, vol. 1426, pp. 991-994, 2012.
- [14] S. V. Razorenov, G. I. Kanel', G. V. Garkushin, and O. N. Ignatova, "Resistance to dynamic deformation and fracture of tantalum with different grain and defect structures," *Physics of the Solid State*, vol. 54, pp. 790-797, 2012/04/01 2012.
- [15] J. R. Asay, T. Ao, T. J. Vogler, J.-P. Davis, and G. T. G. III, "Yield strength of tantalum for shockless compression to 18 GPa," *Journal of Applied Physics*, vol. 106, p. 073515, 2009.
- [16] J. L. Brown, C. S. Alexander, J. R. Asay, T. J. Vogler, D. H. Dolan, and J. L. Belof, "Flow strength of tantalum under ramp compression to 250 GPa," *Journal of Applied Physics*, vol. 115, p. 043530, 2014.

- [17] J.-P. Davis, J. L. Brown, M. D. Knudson, and R. W. Lemke, "Analysis of shockless dynamic compression data on solids to multi-megabar pressures: Application to tantalum," *Journal of Applied Physics*, vol. 116, p. 204903, 2014.
- [18] J. L. Ding, J. R. Asay, and T. Ao, "Modeling of the elastic precursor behavior and dynamic inelasticity of tantalum under ramp wave loading to 17 GPa," *Journal of Applied Physics*, vol. 107, p. 083508, 2010.
- [19] J. H. Eggert, R. F. Smith, D. C. Swift, R. E. Rudd, D. E. Fratanduono, D. G. Braun, et al., "Ramp compression of tantalum to 330 GPa," *High Pressure Research*, vol. 35, pp. 339-354, 2015/10/02 2015.
- [20] N. W. Moore, C. A. McCoy, D. Dolan, B. Fox, A. Vackel, R. Hohlfelder, et al., "Experimental Platforms for Thermomechanical Shock in Advanced Materials," Sandia National Laboratories, Albuquerque, NM SAND2019-11820, 2019.
- [21] T. Van Steenkiste and D. W. Gorkiewicz, "Analysis of tantalum coatings produced by the kinetic spray process," *Journal of Thermal Spray Technology*, vol. 13, pp. 265-273, June 01 2004.
- [22] J. A. Gan and C. C. Berndt, "Review on the Oxidation of Metallic Thermal Sprayed Coatings: A Case Study with Reference to Rare-Earth Permanent Magnetic Coatings," *Journal of Thermal Spray Technology*, vol. 22, pp. 1069-1091, 2013.
- [23] S. M. Cardonne, P. Kumar, C. A. Michaluk, and H. D. Schwartz, "Tantalum and its alloys," *International Journal of Refractory Metals and Hard Materials*, vol. 13, pp. 187-194, 1995/01/01/1995.
- [24] V. V. Sobolev and J. M. Guilemany, "Effect of oxidation on droplet flattening and splat-substrate interaction in thermal spraying," *Journal of Thermal Spray Technology*, vol. 8, pp. 523-530, 1999/12/01 1999.
- [25] V. V. Sobolev and J. M. Guilemany, "Flattening of droplets and formation of splats in thermal spraying: A review of recent work—Part 1," *Journal of Thermal Spray Technology*, vol. 8, pp. 87-101, 1999/03/01 1999.
- [26] V. V. Sobolev and J. M. Guilemany, "Flattening of droplets and formation of splats in thermal spraying: A review of recent work—Part 2," *Journal of Thermal Spray Technology*, vol. 8, pp. 301-314, 1999/06/01 1999.
- [27] C. Hampel, "Refractory Metals. Tantalum, Niobium, Molybdenum, Rhenium, and Tungsten," *Industrial & Engineering Chemistry*, vol. 53, pp. 90-96, 1961/02/01 1961.
- [28] W. H. Kohl, Handbook of Materials and Techniques for Vacuum Devices. New York: Reinhold, 1967.
- [29] T. Ao, J. R. Asay, S. Chantrenne, M. R. Baer, and C. A. Hall, "A compact strip-line pulsed power generator for isentropic compression experiments," *Review of Scientific Instruments*, vol. 79, p. 013903, 2008.
- [30] L. M. Barker and R. E. Hollenbach, "Laser Interferometer for Measuring High Velocities of Any Reflecting Surface," *J. Appl. Phys.*, vol. 43, pp. 4669–4675, 1972.
- [31] L. M. Barker and K. W. Schuler, "Correction to the Velocity-Per-Fringe Relationship for the VISAR Interferometer," *J. Appl. Phys.*, vol. 45, pp. 3692–3693, 1974.
- [32] D. H. Dolan and S. C. Jones, "Push-pull analysis of photonic Doppler velocimetry measurements," *Review of Scientific Instruments*, vol. 78, p. 076102, 2007.
- [33] B. J. Jensen, D. B. Holtkamp, P. A. Rigg, and D. H. Dolan, "Accuracy limits and window corrections for photon Doppler velocimetry," *Journal of Applied Physics*, vol. 101, p. 013523, 2007.
- [34] D. H. Dolan, "Foundations of VISAR analysis," Sandia National Laboratories, Albuquerque, NM SAND2006-1950, 2006.

- [35] T. Ao and D. H. Dolan, "SIRHEN: a data reduction program for photonic Doppler velocimetry measurements," Sandia National Laboratories SAND2010-3628, 2010.
- [36] E. Z. Wang and N. G. Shrive, "A 3-D ellipsoidal flaw model for brittle fracture in compression," *International Journal of Solids and Structures*, vol. 36, pp. 4089-4109, 1999/09/01/1999.
- [37] W. T. Becker, "Ductile and Brittle Fracture," ASM International, Materials Park, OH, USA1992.
- [38] A. Pineau, A. A. Benzerga, and T. Pardoen, "Failure of metals I: Brittle and ductile fracture," *Acta Materialia*, vol. 107, pp. 424-483, 2016/04/01/2016.
- [39] J.-Y. Kim, D. Jang, and J. R. Greer, "Tensile and compressive behavior of tungsten, molybdenum, tantalum and niobium at the nanoscale," *Acta Materialia*, vol. 58, pp. 2355-2363, 2010/04/01/2010.
- [40] N. W. Moore, C. C. Battaile, J. B. Carleton, A. J. Olson, T. Rodgers, A. Vackel, *et al.*, "Stochastic shock in Porous Refractory Metals," Sandia National Laboratories, Albuquerque, NM SAND2019-14283, 2019.
- [41] D. B. Reisman, B. S. Stoltzfus, W. A. Stygar, K. N. Austin, E. M. Waisman, R. J. Hickman, et al., "Pulsed power accelerator for material physics experiments," *Physical Review Special Topics Accelerators and Beams*, vol. 18, p. 090401, 09/09/2015.

APPENDIX A. WAVEFORM DATA

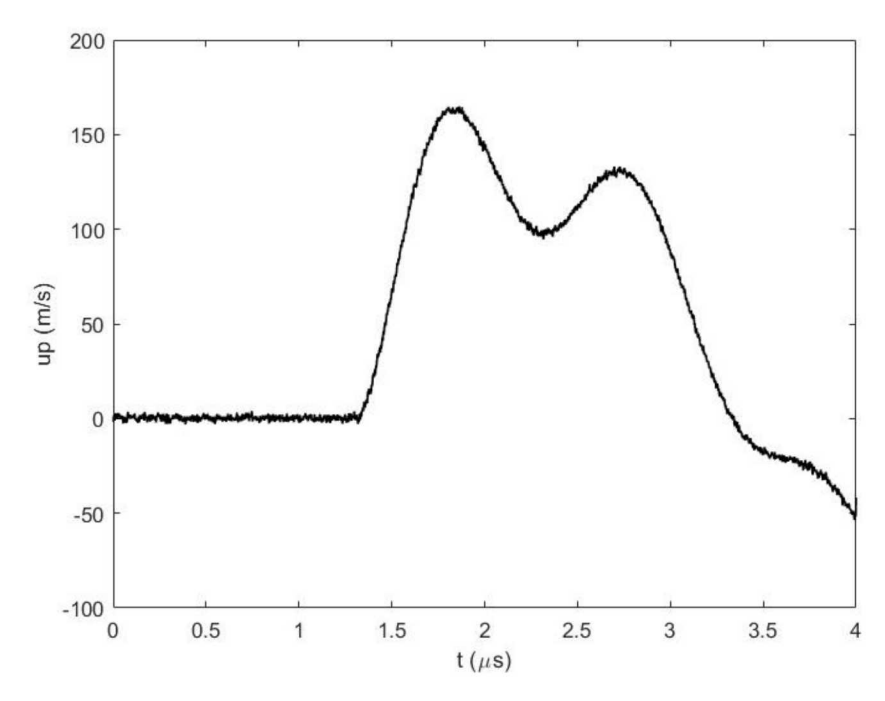


Figure A-1: Measured velocity profile in sapphire window for shot V543.

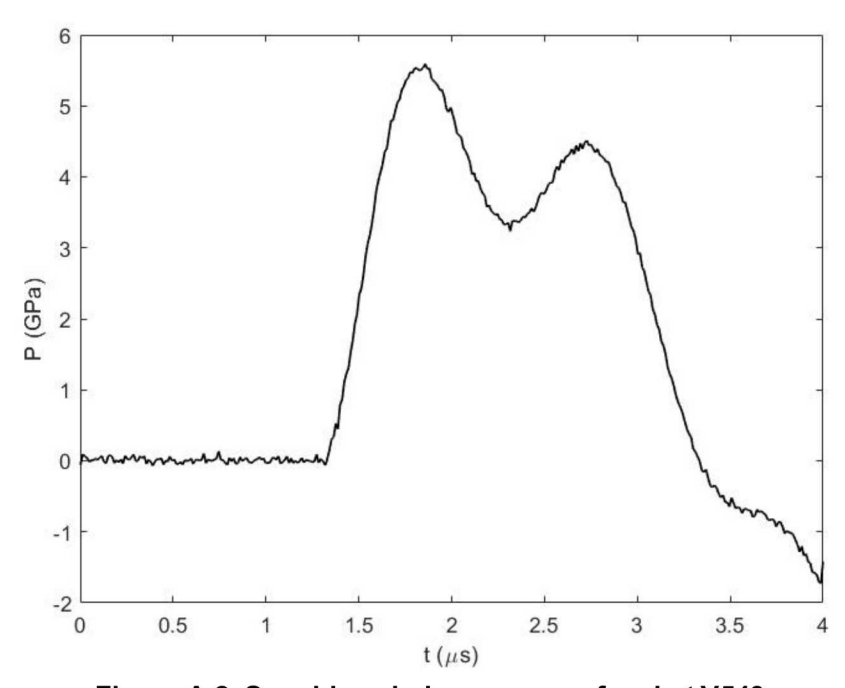


Figure A-2: Sapphire window pressure for shot V543.

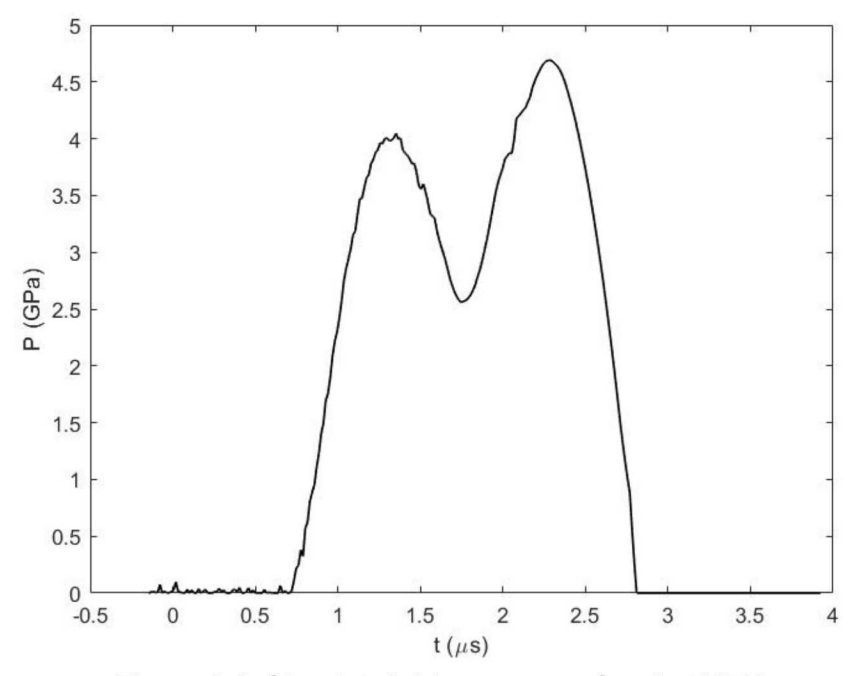


Figure A-3: Simulated drive pressure for shot V543.

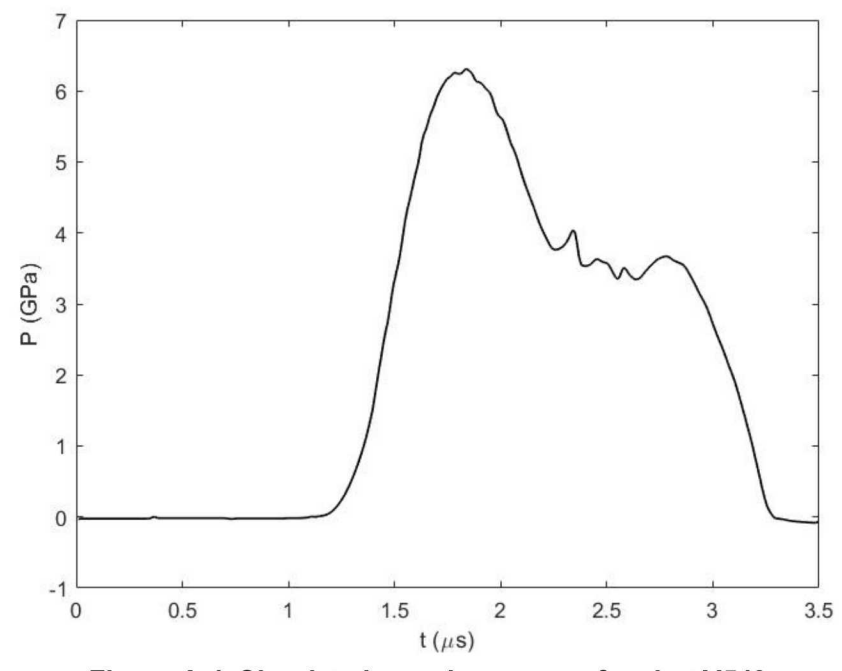
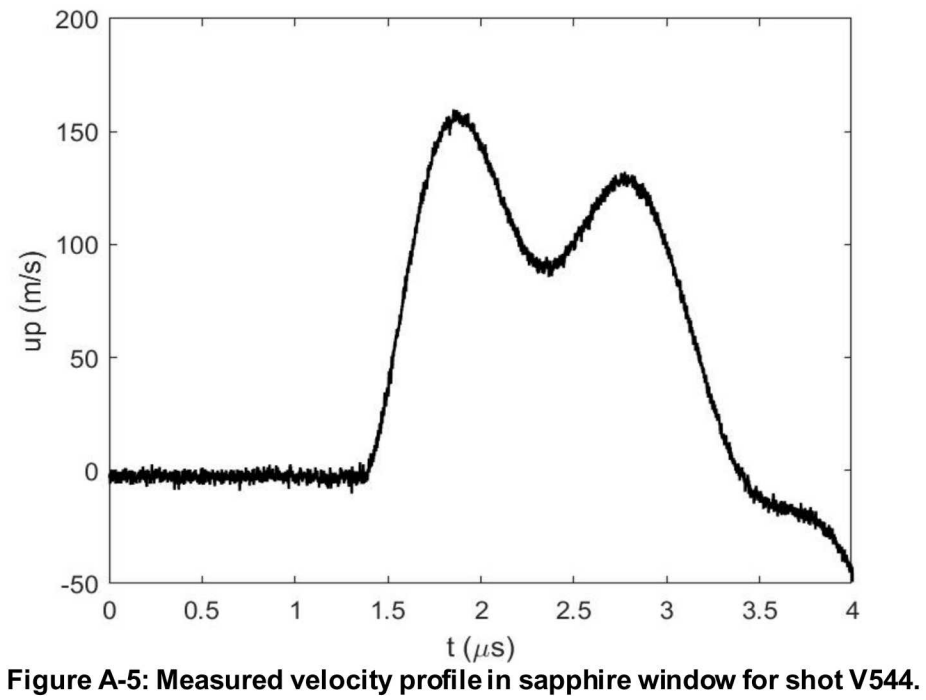


Figure A-4: Simulated sample pressure for shot V543.



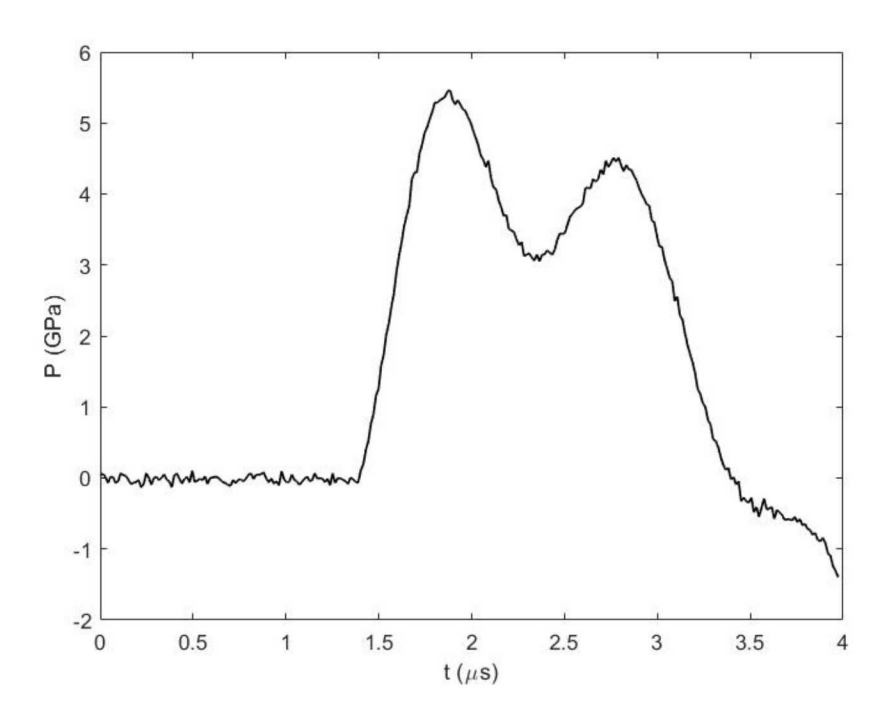


Figure A-6: Sapphire window pressure for shot V544.

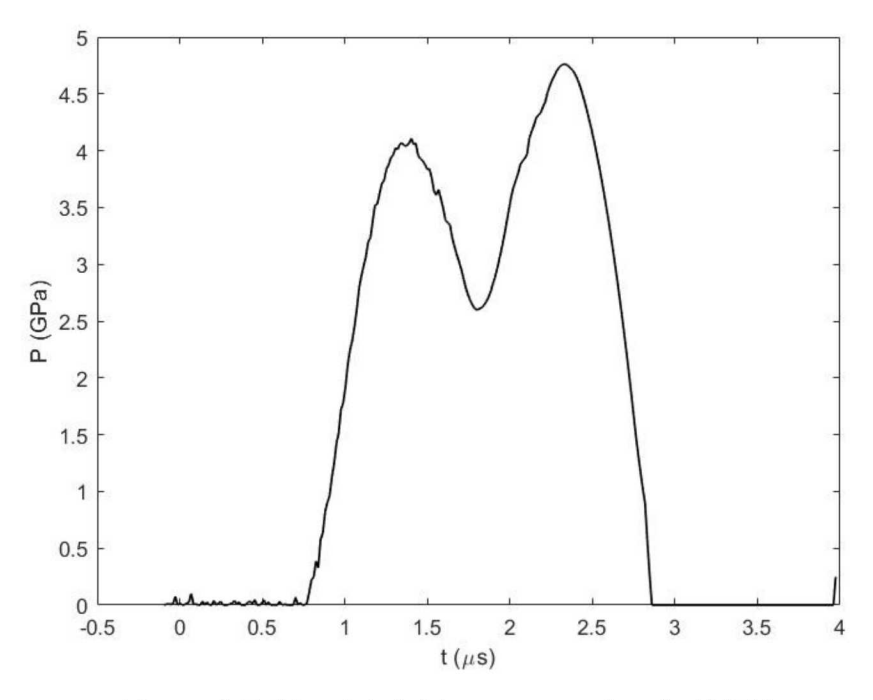


Figure A-7: Simulated drive pressure for shot V544.

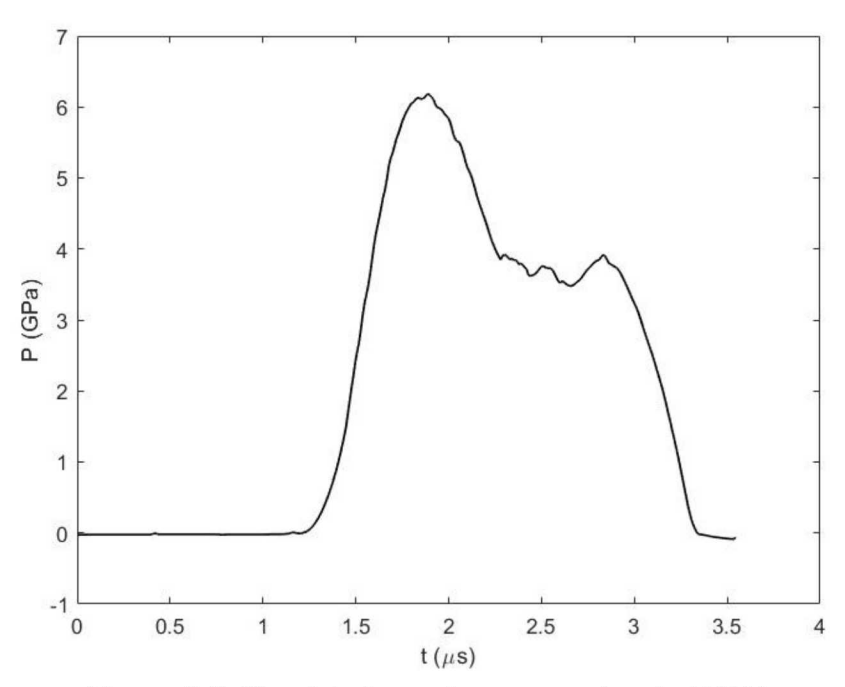


Figure A-8: Simulated sample pressure for shot V544.

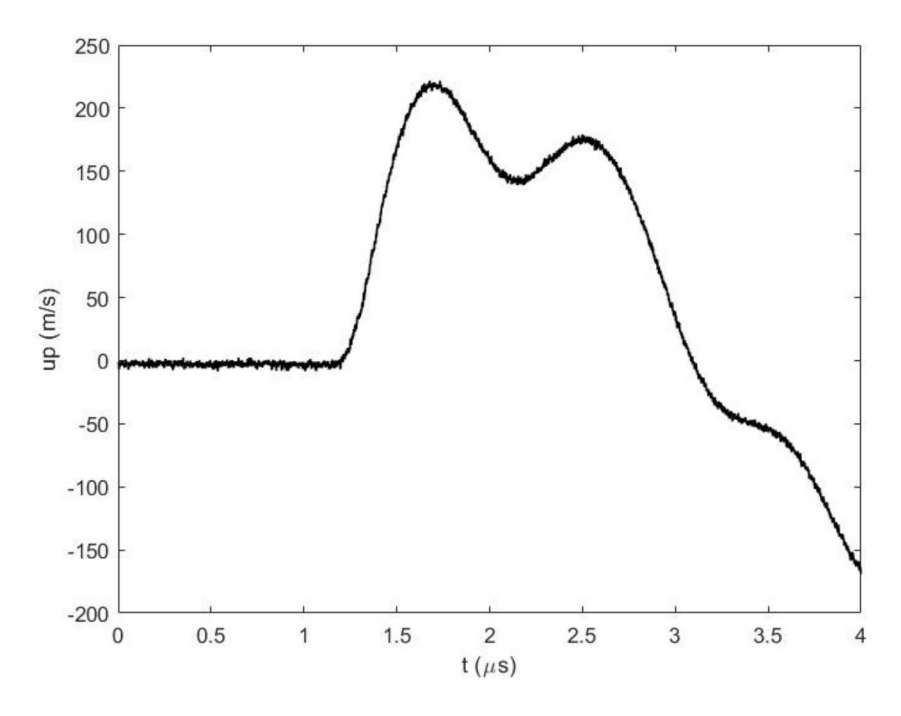


Figure A-9: Measured velocity profile in sapphire window for shot V545.

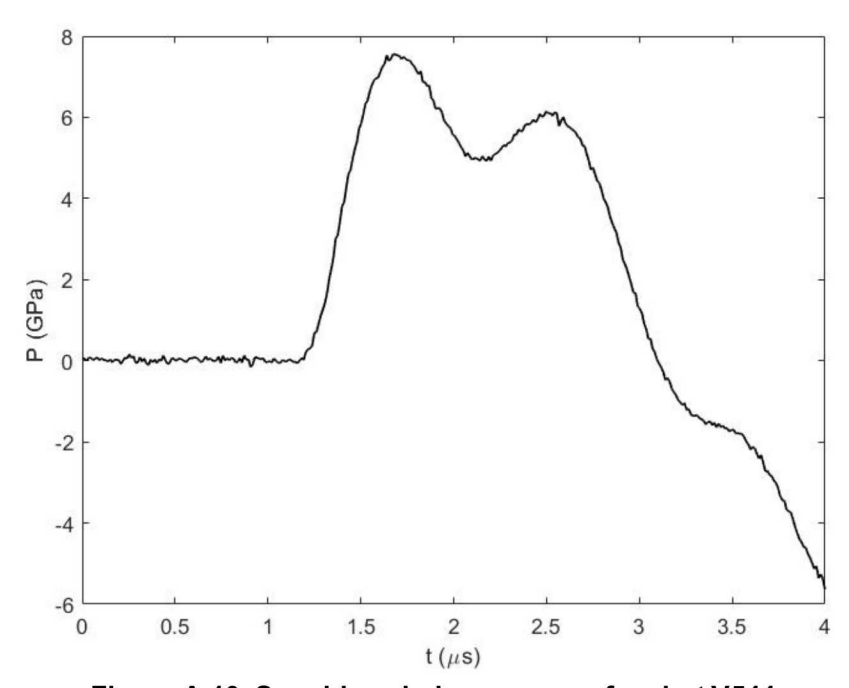


Figure A-10: Sapphire window pressure for shot V544.

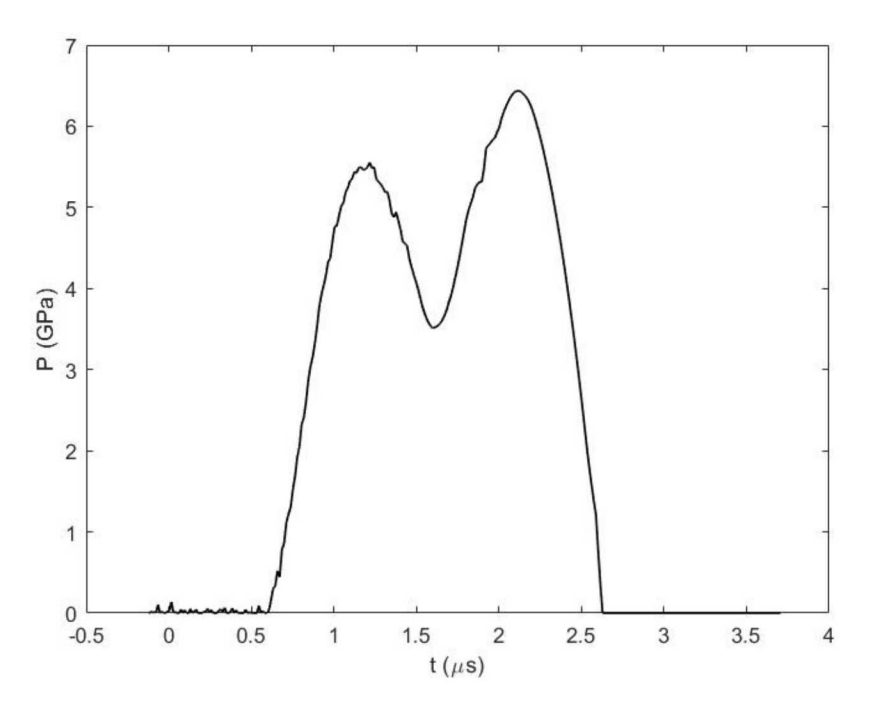


Figure A-11: Simulated drive pressure for shot V545.

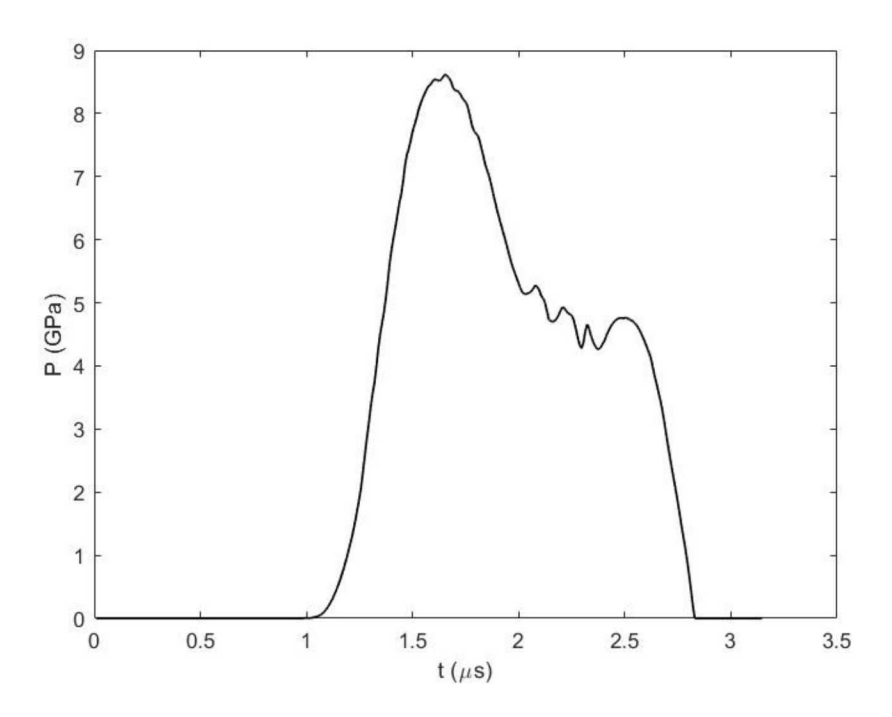


Figure A-12: Simulated sample pressure for shot V545.

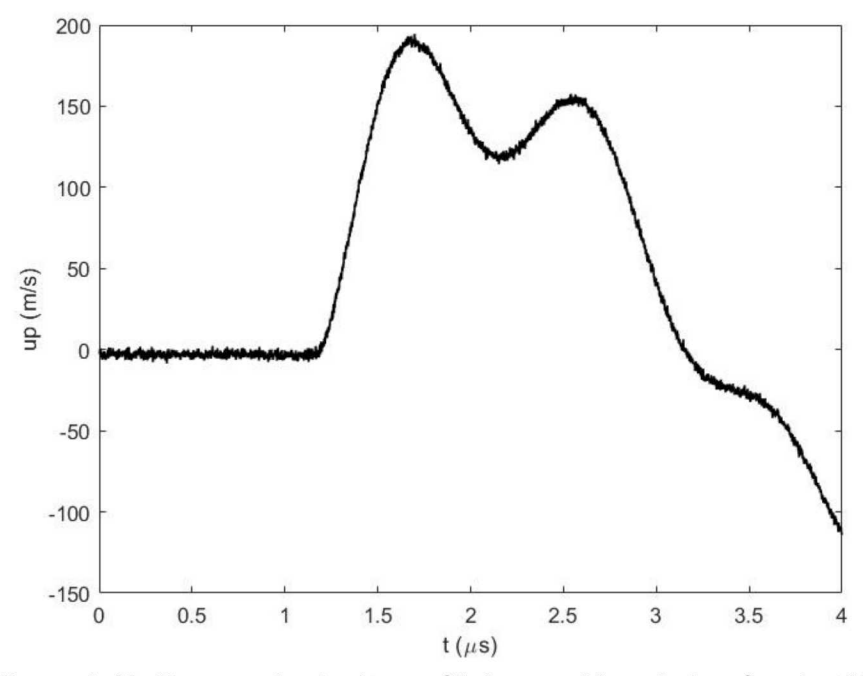


Figure A-13: Measured velocity profile in sapphire window for shot V546.

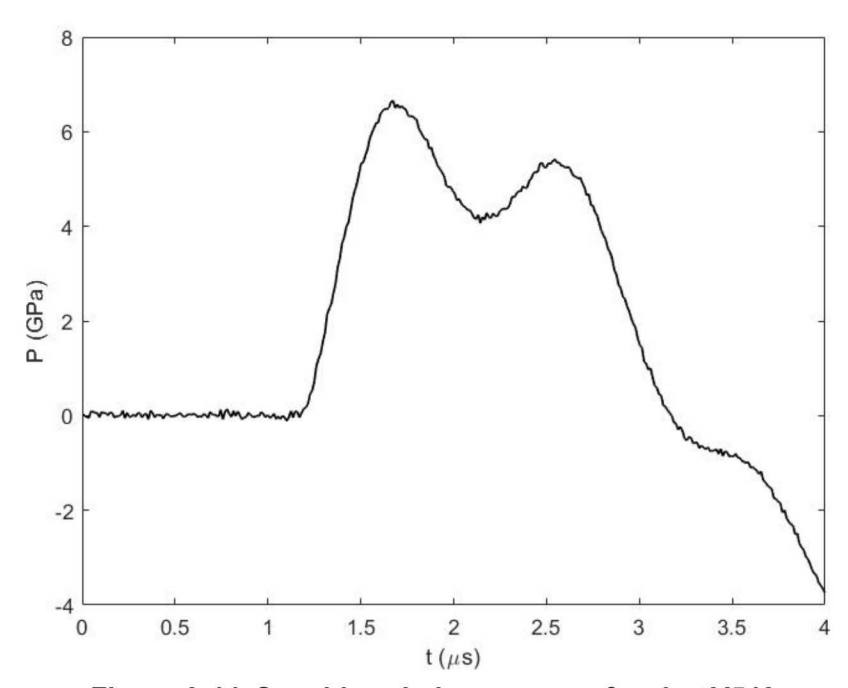


Figure A-14: Sapphire window pressure for shot V546.

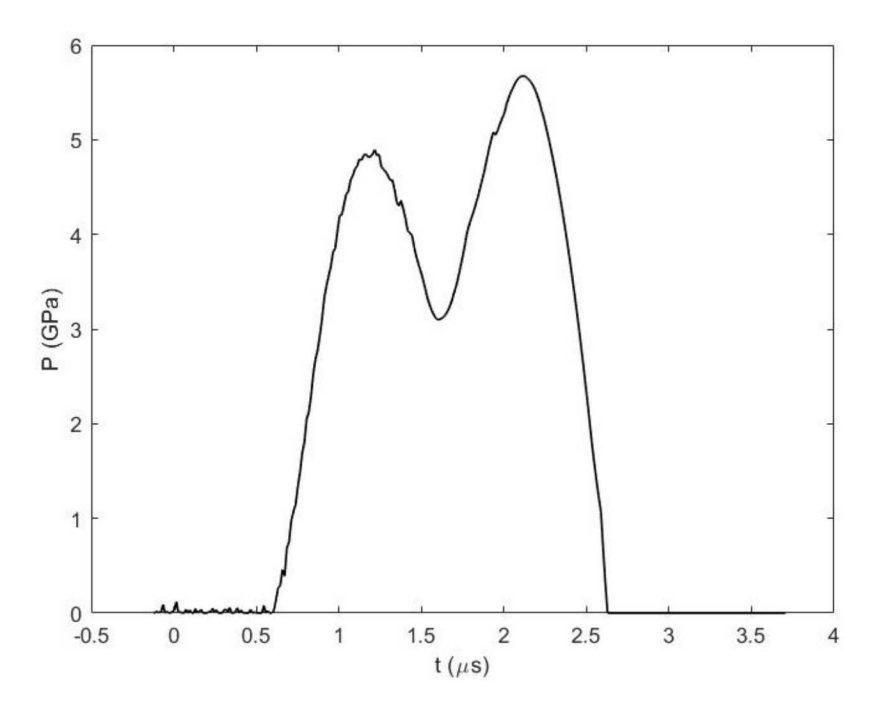


Figure A-15: Simulated drive pressure for shot V546.

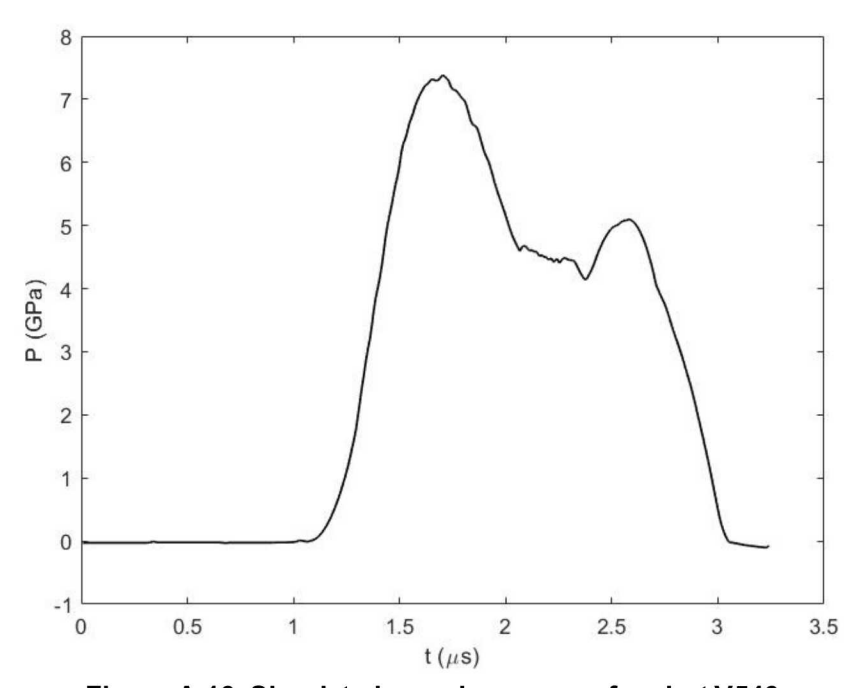


Figure A-16: Simulated sample pressure for shot V546.

APPENDIX B. OVERVIEW IMAGES

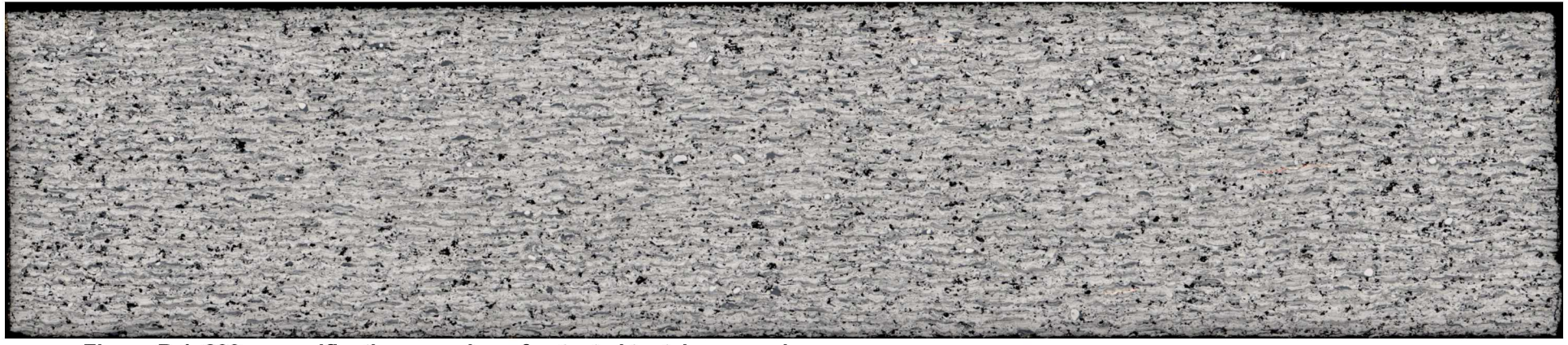


Figure B-1: 200x magnification overview of untested tantalum sample



Figure B-2: 200x magnification overview of V543 tantalum sample compressed to 6.3 GPa

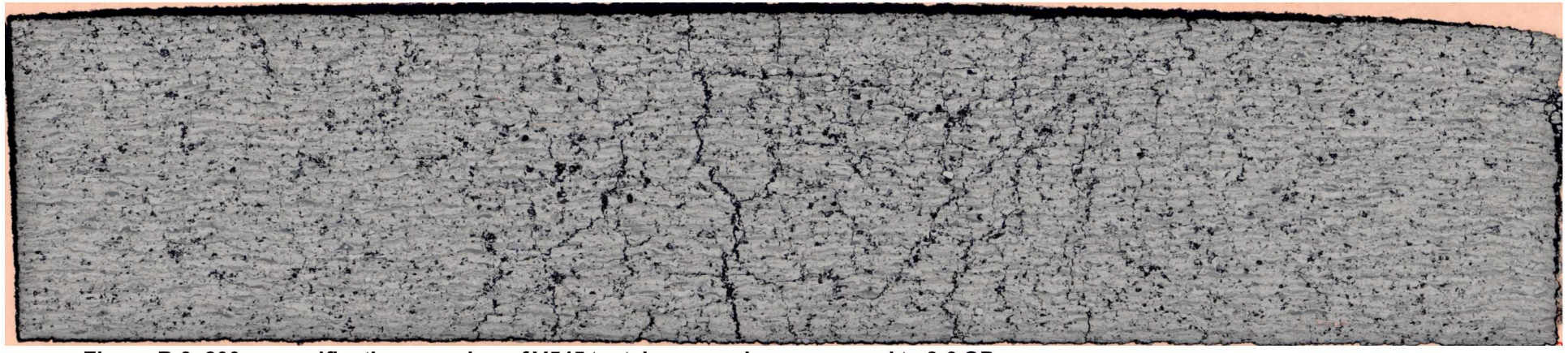


Figure B-3: 200x magnification overview of V545 tantalum sample compressed to 8.6 GPa



Figure B-4: 200x magnification overview of untested tantalum-niobium sample



Figure B-5: 200x magnification overview of V544 tantalum-niobium sample compressed to 6.2 GPa



Figure B-6: 200x magnification overview of V546 tantalum-niobium sample compressed to 7.4 GPa

This page left blank

DISTRIBUTION

Email—Internal

Name	Org.	Sandia Email Address	
Bryan Oliver	1340	bvolive@sandia.gov	
Shawn Pautz	1341	sdpautz@sandia.gov	
Aaron Olson	1341	aolson@sandia.gov	
Nathan Moore	1344	nwmoore@sandia.gov	
James Bryson	1344	iwbryso@sandia.gov	
James Carleton	1443	jbcarle@sandia.gov	
Mikhail Mesh	1553	mmesh@sandia.gov	
Bill Scherzinger	1558	wmscher@sandia.gov	
Brittany Branch	1646	babranc@sandia.gov	
Chad McCoy	1646	camccoy@sandia.gov	
Chris Seagle	1646	ctseagl@sandia.gov	
Steven Dean	1647	swdean@sandia.gov	
Joe Fonseca	1834	<u>icfonse@sandia.gov</u>	
Andrew Vackel	1834	avackel@sandia.gov	
Corbett Battaile	1864	ccbatta@sandia.gov	
Theron Rodgers	1864	trodger@sandia.gov	
Aaron Hall	5814	achall@sandia.gov	
John Sullivan	8425	jpsulli@sandia.gov	
Technical Library	1977	sanddocs@sandia.gov	



Sandia National Laboratories is a multimission laboratory managed and operated by National Technology & Engineering Solutions of Sandia LLC, a wholly owned subsidiary of Honeywell International Inc. for the U.S. Department of Energy's National Nuclear Security Administration under contract DE-NA0003525.